In Vivo Integrity and Biological Fate of Chelator-Free Zirconium-89-Labeled Mesoporous Silica Nanoparticles

Feng Chen,[†,⊥] Shreya Goel,[‡,⊥] Hector F. Valdovinos,[§] Haiming Luo,[†] Reinier Hernandez,[§] Todd E. Barnhart,[§] and Weibo Cai*,[†,‡,§,∥]

[†]Department of Radiology, [‡]Materials Science Program, and [§]Department of Medical Physics, University of Wisconsin, Madison, Wisconsin 53705, United States and [∥]University of Wisconsin Carbone Cancer Center, Madison, Wisconsin 53705, United States. [⊥]F.C. and S.G. contributed equally to this work

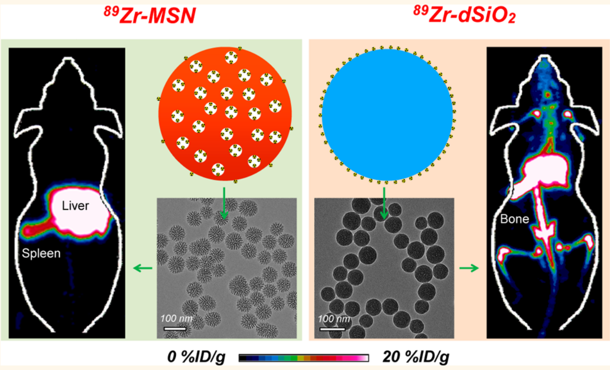

ABSTRACT Traditional chelator-based radio-labeled nanoparticles and positron emission tomography (PET) imaging are playing vital roles in the field of nano-oncology. However, their long-term *in vivo* integrity and potential mismatch of the biodistribution patterns between nanoparticles and radio-isotopes are two major concerns for this approach. Here, we present a chelator-free zirconium-89 (^{89}Zr, $t_{1/2}$ = 78.4 h) labeling of mesoporous silica nanoparticle (MSN) with significantly enhanced *in vivo* long-term (>20 days) stability. Successful radio-labeling and *in vivo* stability are demonstrated to be highly dependent on both the concentration and location of deprotonated silanol groups ($-\mathrm{Si}-\mathrm{O}^{-}$) from two types of silica nanoparticles investigated. This work reports ^{89}Zr-labeled MSN with a detailed labeling mechanism investigation and long-term stability study. With its attractive radio-stability and the simplicity of chelator-free radio-labeling, ^{89}Zr-MSN offers a novel, simple, and accurate way for studying the *in vivo* long-term fate and PET image-guided drug delivery of MSN in the near future.

KEYWORDS: zirconium-89 · mesoporous silica nanoparticle · chelator-free radio-labeling · positron emission tomography

Positron emission tomography (PET) is a highly sensitive and noninvasive imaging modality, which is playing a vital role in nano-oncology for assessing the quantitative tumor uptake and studying the pharmacokinetic (PK) profiles of radio-labeled nanoparticles in live animals.[1,2] To date, chelator-based radio-labeling is still the most widely used technique for the synthesis of various kinds of radio-labeled nanoparticles. For example, copper-free click chemistry has been developed to attach fluorine-18 (^{18}F, $t_{1/2}$ = 109 min) to porous silica nanoparticles.[3,4] By using either NOTA (1,4,7-triazacyclononane-1,4,7-triacetic acid) or DOTA (1,4,7,10-tetraazacyclododecane-1,4,7,10-tetraaceticacid) as the chelator, copper-64 (^{64}Cu, $t_{1/2}$ = 12.7 h)-labeled carbon nanotubes,[5] quantum dots,[6] superparamagnetic iron oxide nanoparticles (SPIONs),[7] porous silica nanoparticles,[8,9] to name a few, have also been reported and used for tumor-targeted cancer imaging and biodistribution studies.

Despite the high sensitivity and no limitation in tissue penetration of signal, radio-labeled nanoparticles still provoke concerns of their *in vivo* (long-term) integrity (or stability).[10] For example, dissociation of free ^{64}Cu (or ^{64}Cu-DOTA) and significant bladder uptake have been reported during the *in vivo* PET imaging of ^{64}Cu-DOTA-PEG-Au.[11] It is worthy to mention that the nanoparticle itself is not a positron emitter, and PET imaging only detects signals from the radio-isotopes (which usually are linked to the nanoparticle with a selected chelator as the bridge). Most free radio-isotopes (or isotopes stabilized by chelators) do not share the same PK profile with the nanoparticle of interest. Potential detachment of these radio-isotopes from nanoparticles *in vivo* could easily lead to erroneous interpretation of PET imaging results.

To address these concerns, there is an emerging concept of synthesizing intrinsically radio-labeled nanoparticles for more

* Address correspondence to wcai@uwhealth.org.

Received for review January 23, 2015 and accepted July 25, 2015.

10.1021/acsnano.5b00526

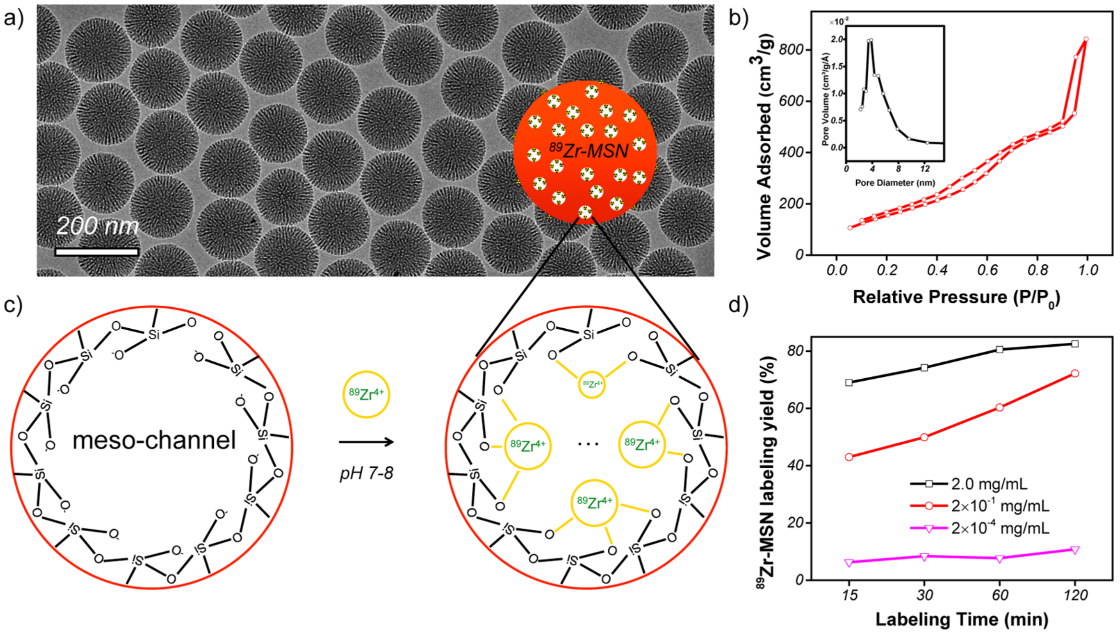

Figure 1. Chelator-free ^{89}Zr labeling of MSN. (a) TEM image of MSN with an average particle size of ~150 nm. (b) Nitrogen adsorption–desorption isotherms and the corresponding pore size distributions of MSN. (c) Schematic illustration showing the labeling of $^{89}Zr^{4+}$ to the deprotonated silanol groups (–Si–O$^-$) from the outer surface and inner meso-channels of MSN. (d) Time-dependent ^{89}Zr labeling yield in HEPES buffer solution (pH 7–8) with varied MSN concentrations (from 2 mg/mL to 2 × 10^{-4} mg/mL).

accurate investigation of the nanoparticle's PK profile *in vivo*.[12] Successful synthesis of intrinsically radio-labeled nanoparticle lies in the strong interaction between rationally selected nanoparticles and radio-isotopes.[12] Interesting combinations, such as ^{64}Cu-labeled porphysome,[13] arsenic-72 (^{72}As, $t_{1/2}$ = 26 h), and germanium-69 (^{69}Ge, $t_{1/2}$ = 39.1 h)-labeled SPION,[14,15] [^{64}Cu]CuS nanoparticles,[16] ^{18}F-labeled upconversion nanoparticles and hydroxyapatite,[17,18] *etc*., have been reported over the last several years. Although still in the early stages, design and synthesis of intrinsically radio-labeled nanoparticles have shown an attractive potential in offering an easier, faster, more stable, and more specific radio-labeling technique for the next generation of nano-oncology.

Zirconium-89 (^{89}Zr, $t_{1/2}$ = 78.4 h) is a radio-isotope with a relatively low positron energy (β^{+}_{avg} = 395.5 keV), which is highly suitable for long blood circulating monoclonal antibody (mAb)-based PET imaging.[19] Importantly, translational research of ^{89}Zr-based agents is now under active development with at least five clinical trials ongoing in the USA alone (many more in Europe).[20] Desferrioxamine B (DFO), a hexadentate ligand with three hydroxamate groups that provide six oxygen donors for metal binding, is currently the preferred chelator for labeling of $^{89}Zr^{4+}$.[21–25] However, significant bone uptake of ^{89}Zr (3–15 %ID/g) was still observed for various ^{89}Zr-DFO-mAb studies within 7 days postinjection (p.i.),[22–25] indicating the release of free ^{89}Zr and limited stability of DFO-based ^{89}Zr labeling.

Mesoporous silica nanoparticles (MSNs) with controllable mesoporous structure, high specific surface area, and large pore volume have attracted increasing interest as drug delivery nanosystems.[26] The presence of abundant silanol groups (–Si–OH) on the silica surface has been well-known for many decades.[27] However, this has not been considered for potential radio-labeling until now.

In this work, we hypothesize that numerous deprotonated silanol groups (–Si–O$^-$) inside the meso-channels or on the surface of MSN could function as inherent hard oxygen donors for stable radio-labeling of ^{89}Zr. By using an amorphous dense silica nanoparticle as a control, our systematic research demonstrated a significantly enhanced stability of ^{89}Zr-MSN in mice over 3 weeks (~7 $t_{1/2}$ of ^{89}Zr). This study provides a chelator-free labeling mechanism for mesoporous silica nanoparticles to study their long-term *in vivo* stability and fate.

RESULTS AND DISCUSSION

MSN Synthesis and Characterization. Zr^{4+} is a hard Lewis acid and thus prefers hard Lewis bases as donor groups. It has been known for many decades that, during the hydrolysis and condensation of tetraethyl orthosilicate (TEOS), abundant silanol groups (–Si–OH) form on the surface of amorphous silica particles.[27] Here, we demonstrate that it is the deprotonated silanol groups (–Si–O$^-$) that function as the hard Lewis bases for the successful chelator-free ^{89}Zr labeling of amorphous silica nanoparticles.

As seen in Figure 1a, a uniform MSN with an average particle size of ~150 nm in diameter was synthesized using literature procedures.[28] The presence of radial meso-channels throughout each MSN could be easily seen from the transmission electron microscopy (TEM) image. Nitrogen adsorption–desorption isotherms further confirmed an obvious capillary condensation step at P/P_0 around 0.4 (Figure 1b), which is clear evidence for the presence of mesopores in MSN. The second adsorption of the isotherms at high relative pressure ($P/P_0 > 0.8$) represents the formation of interstitial pores among the dried MSN agglomerates (also known as textural porosity). The Brunauer–Emmett–Teller (BET) surface area was measured to be 581.5 m^2/g, with a high pore volume of 1.3 cm^3/g. Pore size distribution showed an average pore size of 4–5 nm (Figure 1b, inset), consistent with the previously reported values.[28]

According to the Zhuravlev model, for both porous and nonporous silica particles, the concentrations of silanol groups are directly proportional to the specific surface area, with the density ($-Si-OH/nm^2$) found to be in the range of 4–5 (also known as the Kiselev–Zhuravlev constant).[27] About 2–3 million $-Si-OH$ groups in each MSN particle were estimated based on our calculation (detailed in Supporting Information, Table S1). Considering that over 95% of the surface in MSN is internal mesopore surface based on a recent hemolysis study of MSN,[29] nearly all of the $-Si-OH$ groups are expected to be inside the meso-channels but not on MSN's outer surface, as schematically shown in Figure 1c.

These silanol groups ($-Si-OH$) can be fully deprotonated to become $-Si-O^-$ when the pH value of aqueous solution is higher than the isoelectric point of silica, which has been known to be in the range of pH 2–3. Our ζ-potential analysis confirmed the negatively charged surface of as-synthesized MSN (−48.4 ± 0.3 mV) in water (pH 7–8), suggesting the presence of $-Si-O^-$ groups on MSN surface.

Chelator-Free ^{89}Zr Labeling. Our results showed that about 70% ^{89}Zr labeling yield was achieved for MSN within the first 15 min of incubation (Table S2). The yield continued to increase over time and reached 82.5% at 2 h post-incubation (Figure 1d and Table S2). As expected, ^{89}Zr-labeling was MSN concentration and temperature dependent, where higher concentration and high incubation temperature gave higher labeling yield (Figure 1d, Figure S1, Table S3). We further demonstrated that there was no significant reduction (less than 5%) of drug loading capacity after labeling MSN with ^{89}Zr (Table S4).

To further demonstrate the role of deprotonated silanol groups in ^{89}Zr-labeling, the pH value of MSN in HEPES (0.1 M) was adjusted to 2–3 to ensure protonation of silanol groups (as $-Si-OH$). Such protonation was confirmed by a positively charged surface (3.6 ± 0.3 mV) of MSN at pH 2–3. As expected, ^{89}Zr labeling yield was significantly reduced even at a MSN concentration of 2 mg/mL (Figure S1 and Table S3). With these findings, we demonstrated that deprotonated silanol groups play a vital role in chelator-free labeling of ^{89}Zr to MSN.

***In Vitro* Stability Study of ^{89}Zr-MSN.** To further investigate how the location and concentration of deprotonated silanol groups could affect the ^{89}Zr labeling yield and stability, $dSiO_2$ was used as a control. Amorphous $dSiO_2$ synthesized by a classic Stöber method is known to have no mesopores inside and a significantly lower surface area (~40 m^2/g for $dSiO_2$ with a size of ~90 nm in diameter, Figure S2) when compared with that of MSN (~600 m^2/g in this work).[30] In stark contrast to MSN, very little mesopore surface but a dominant external surface is expected in these $dSiO_2$ nanoparticles, as schematically shown in Figure 2a.

The TEM image in Figure 2b shows successful synthesis of spherically shaped $dSiO_2$ with an average size of ~90 nm in diameter. The surface charge of $dSiO_2$ in pH 7–8 water was also found to be highly negative (−38.9 ± 0.3 mV), confirming the presence of abundant deprotonated silanol groups on the outer surface of $dSiO_2$. In comparison with MSN, about 17-fold less $-Si-O^-$ groups in each $dSiO_2$ was estimated based on their marked difference in specific surface area (Table S1). By using the same labeling protocol, a similar concentration-dependent ^{89}Zr labeling yield was observed (Figure 2c). As expected, we found significantly lower labeling yield at each time point examined when compared with MSN with the same particle concentration (Tables S2 and S5), again demonstrating the vital role of $-Si-O^-$ group concentration during ^{89}Zr labeling.

A DFO challenge study has been reported to demonstrate the stability of ^{89}Zr-labeled nanoparticles.[31] As-synthesized ^{89}Zr-MSN and ^{89}Zr-$dSiO_2$ (suspended in HEPES, 0.1 M, pH 7–8) were mixed with increasing concentrations of DFO, ranging from 0.05 to 5 mM, and incubated at 37 °C under constant shaking. At each time point, a 100k filter was used to separate the formation of possible ^{89}Zr-DFO. As shown in Figure 3a,b, nearly negligible ^{89}Zr detachment was detected for both ^{89}Zr-MSN and ^{89}Zr-$dSiO_2$ within 48 h, demonstrating a strong binding affinity of ^{89}Zr to both silica nanoparticles. The stability of ^{89}Zr-MSN and ^{89}Zr-$dSiO_2$ in complete mouse serum was further tested. ^{89}Zr-labeled nanoparticles were mixed with mouse serum and shaken at 37 °C. Again, no obvious detachment of free ^{89}Zr was observed, with ^{89}Zr-MSN showing slightly better serum stability (Figure 3c). Similar high radiostability (with over 96% ^{89}Zr retained in MSN) has been observed after challenging with EDTA (1 mM) at 37 °C for 7 days (Figure 3d). Taken together, we concluded that both ^{89}Zr-MSN and ^{89}Zr-$dSiO_2$ showed high stability *in vitro*, which encouraged us to test their long-term stabilities *in vivo*.

***In Vivo* Long-Term Stability and Biodistribution Studies.** With a ~3 day half-life, ^{89}Zr-based PET imaging holds

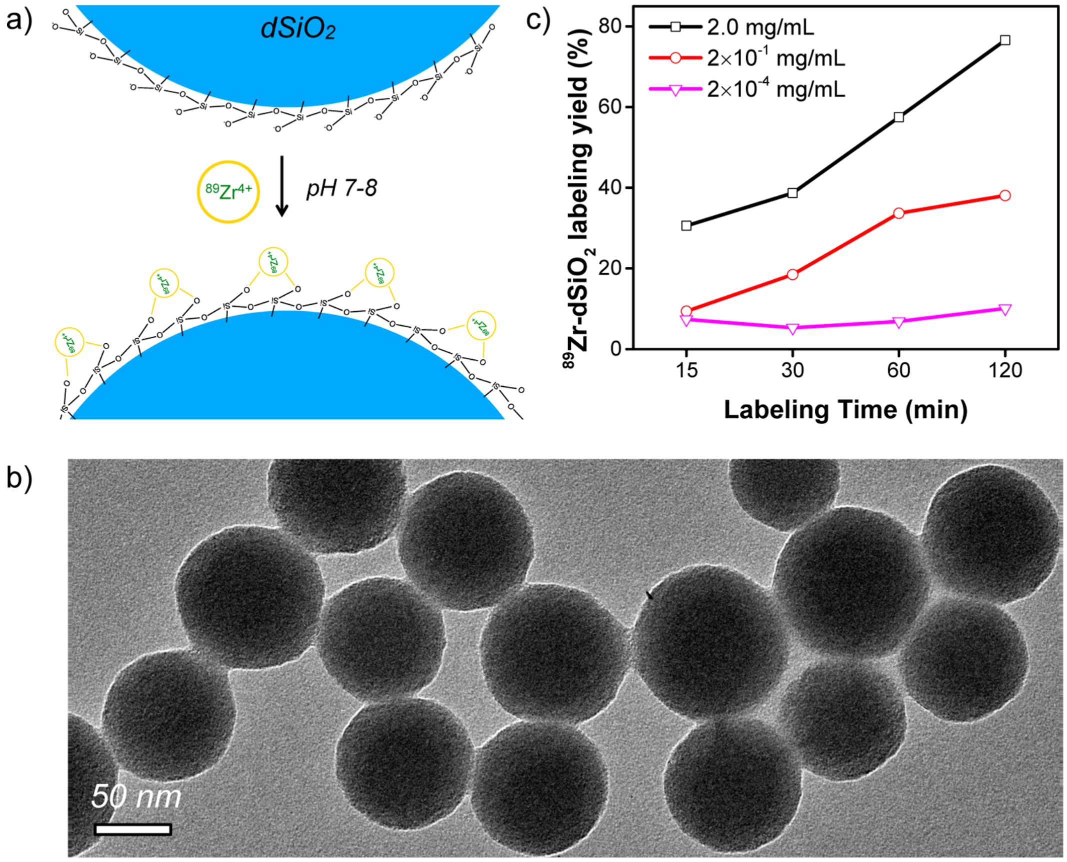

Figure 2. Chelator-free ^{89}Zr labeling of dSiO$_2$. (a) Schematic illustration showing the labeling of ^{89}Zr^{4+} to the deprotonated silanol groups (−Si−O$^-$) from the outer surface of dSiO$_2$. (b) TEM image of dSiO$_2$ with an average particle size of ∼90 nm. (c) Time-dependent ^{89}Zr labeling yield in HEPES buffer solution (pH 7−8) with varied dSiO$_2$ concentrations (from 2 mg/mL to 2 × 10^{-4} mg/mL).

great potential as a useful tool for long-term monitoring of the dynamic biodistribution, biodegradation, clearance pathway, and rate of nanoparticles (or mAbs) *in vivo*. However, a major challenge still exists in developing an optimal chelator for ^{89}Zr labeling. Although our *in vitro* DFO challenge and serum stability studies suggested high stability of ^{89}Zr in both MSN and dSiO$_2$, their ultimate stability needs to be tested *in vivo* for a long period of time.

To do that, healthy BALB/c mice (n = 3) were intravenously (i.v.) injected with ^{89}Zr-MSN or ^{89}Zr-dSiO$_2$ and monitored for 3 weeks (∼7 $t_{1/2}$ of ^{89}Zr). Since detached free ^{89}Zr is a well-known osteophilic cation,[32] with a fast and retained uptake in bones,[33] monitoring the change of bone uptake could be one of the best ways to study the *in vivo* stability of ^{89}Zr-labeled nanoparticles. Our *in vivo* PET and maximum intensity projection images of mice injected with free ^{89}Zr-oxalate (in phosphate-buffered saline, PBS) also confirmed high uptake of ^{89}Zr in the bones and joints, as shown in Figure S3.

Considering that MSN with a larger (*e.g.*, >5 nm) pore size has a faster biodegradation rate in simulated body fluid,[28] in order to potentially visualize the degradation process of ^{89}Zr-MSN using PET imaging, we used ∼90 nm sized MSN with a high surface area (710.7 m^2/g) and 9−10 nm pore size (Figure 4) in the *in vivo* stability study (Figure 5). Normal dSiO$_2$ with a similar particle size served as the control group.

TEM images of ^{89}Zr-dSiO$_2$ and ^{89}Zr-MSN (after decay of radio-activity) showed no obvious morphology change after ^{89}Zr labeling (Figure 5c,e). The maximum intensity projection images showed dominant liver and spleen uptake with no obvious bone uptake within 3 h p.i. in both cases (Figure 5d,f). However, mice injected with ^{89}Zr-dSiO$_2$ started to show significant bone uptake (6.5 ± 5.9 %ID/g; n = 3) from day 1 p.i., which increased to 11.1 ± 7.5 %ID/g on day 3 p.i. (video S1), indicating that the exposed ^{89}Zr from the dSiO$_2$ surface can be vulnerable to attack by the endogenous (protein) ligands. Burst detachment (denoted as stage 1) of free ^{89}Zr from dSiO$_2$ can also be seen in Figure 6a. No further increase in bone uptake and a slow clearance of ^{89}Zr from bone were observed over the next 18 days (denoted as stage 2, Figure 5d, Figure 6a, and Table S6), suggesting a strong binding of the remaining ^{89}Zr on the surface of dSiO$_2$.

Surprisingly, mice injected with ^{89}Zr-MSN showed an extremely high *in vivo* stability throughout 3 weeks, with less than 1 %ID/g uptake in bone on day 7 p.i.

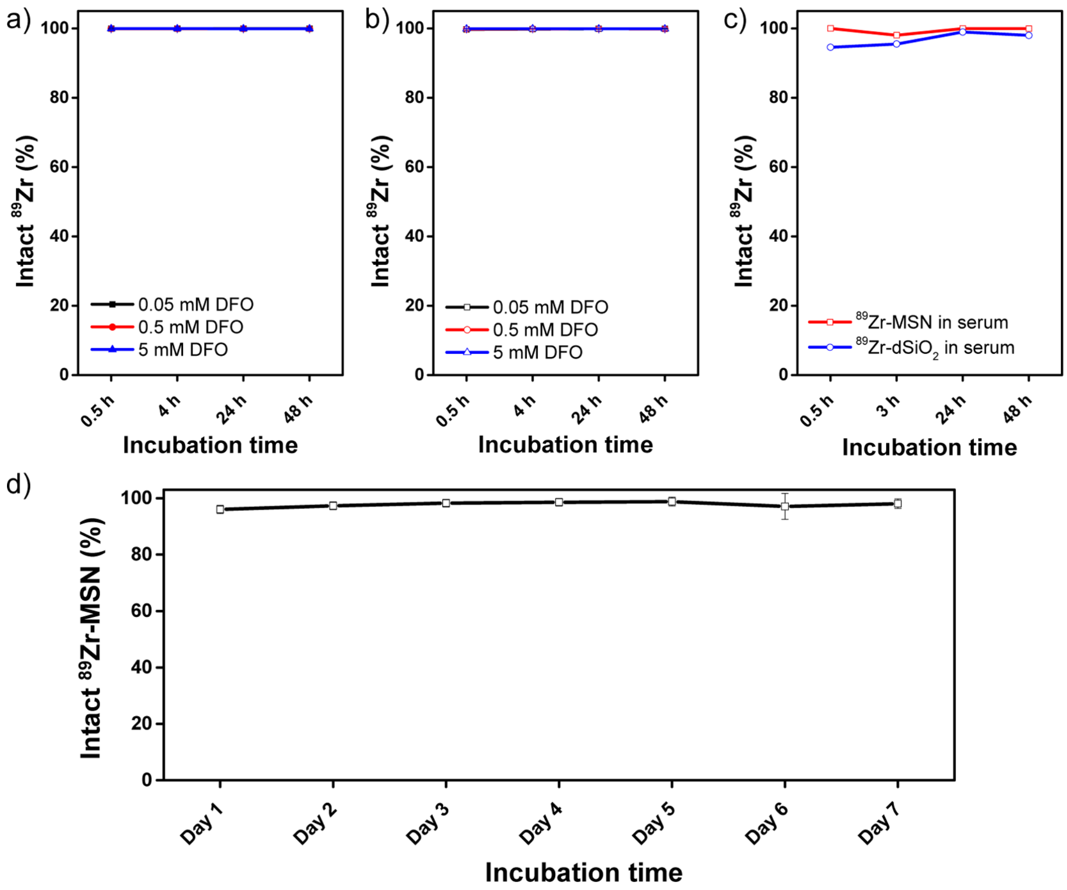

Figure 3. *In vitro* stability of ^{89}Zr-labeled silica nanoparticles. Stability of (a) ^{89}Zr-MSN and (b) ^{89}Zr-dSiO$_2$ when challenged with DFO of varied concentrations from 0.05 to 5 mM at 37 °C for 48 h. (c) Stability of ^{89}Zr-MSN (red line) and ^{89}Zr-dSiO$_2$ (blue line) in whole mouse serum at 37 °C for 48 h. (d) Stability study of ^{89}Zr-MSN when challenged with EDTA (1 mM) at 37 °C for 1 week.

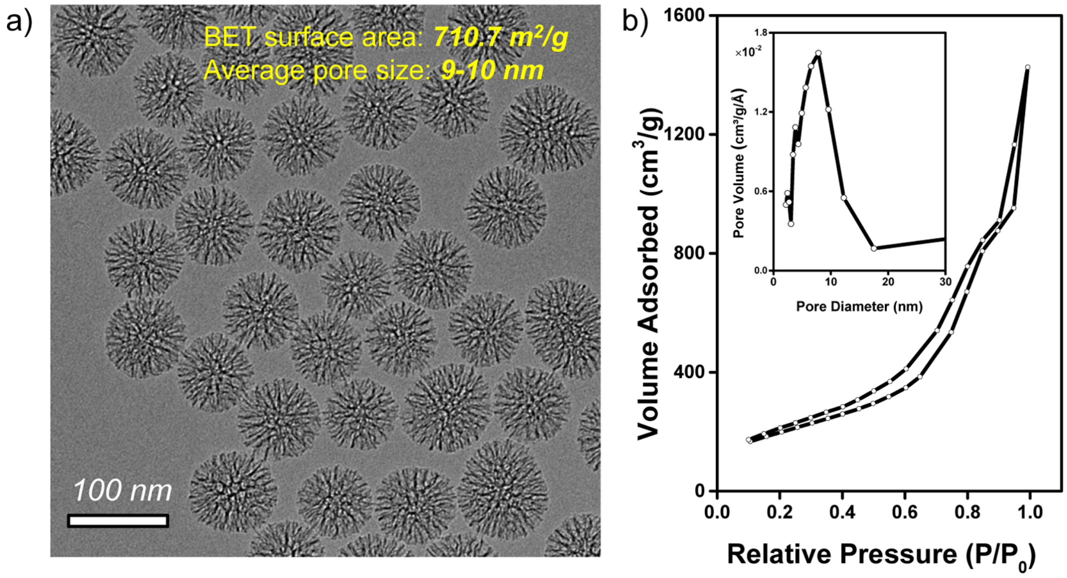

Figure 4. (a) TEM image of MSN with an average particle size of ∼90 nm. (b) Nitrogen adsorption−desorption isotherms and the corresponding pore size distributions of MSN. BET surface area was estimated to be 710.7 m^2/g, and the average pore size was about 9−10 nm.

(video S2), which remains very low at 1.5 ± 0.2 %ID/g at 2 more weeks later (Figure 5h, Figure 6a, and Table S6). The much smaller (but not zero) uptake in bones for ^{89}Zr-MSN may be attributed to the detachment of ^{89}Zr^{4+} ions, which are on the outer surface and not necessarily inside the pores of the MSNs. Such ions

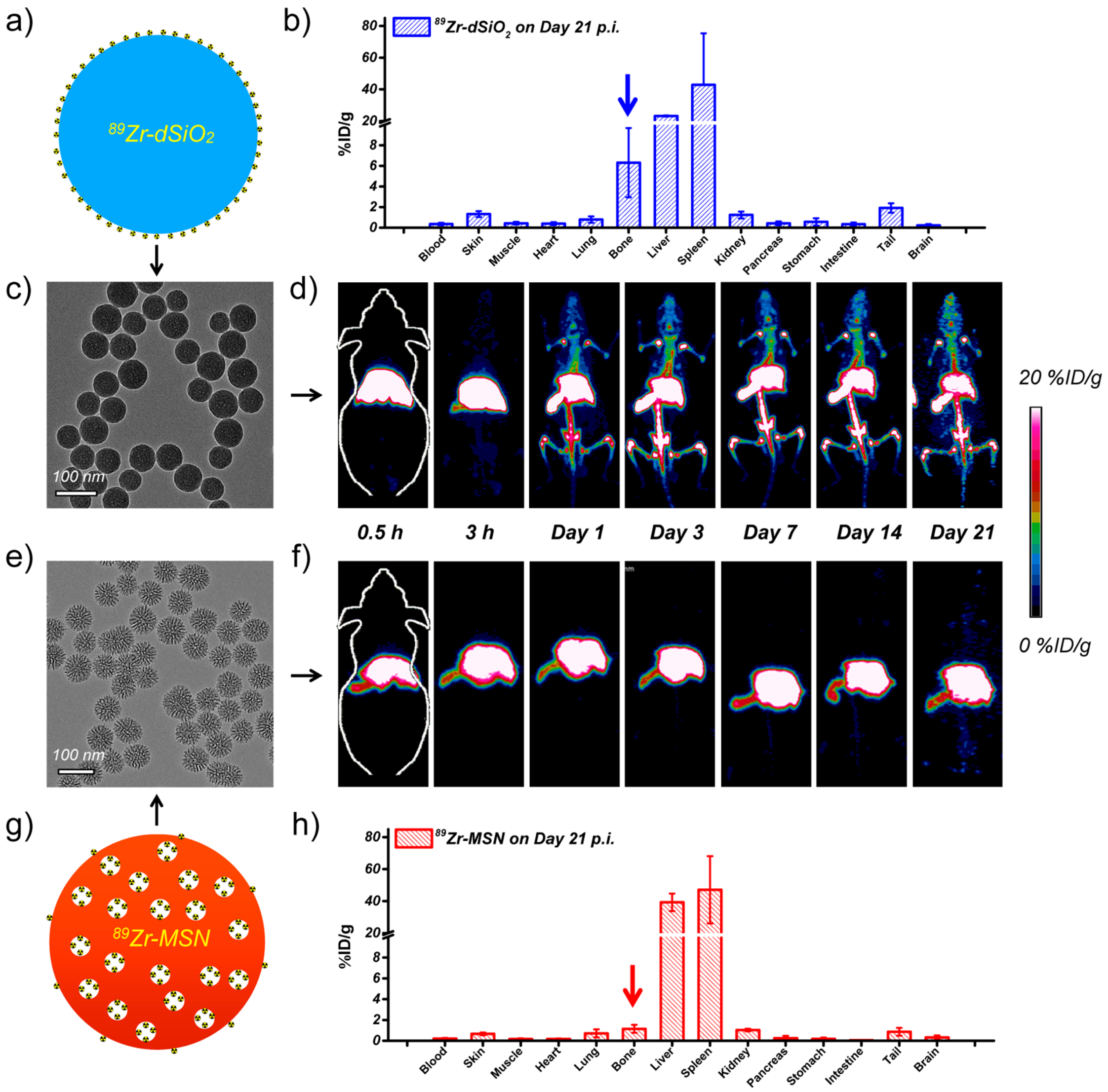

Figure 5. *In vivo* radiostability and *ex vivo* biodistribution studies. (a) Schematic illustration of ^{89}Zr-dSiO$_2$. (b) Biodistribution study of ^{89}Zr-dSiO$_2$ on day 21 p.i. (c) TEM image of ^{89}Zr-dSiO$_2$. (d) *In vivo* serial coronal maximum intensity projection PET images of mice at different time points after i.v. injection of ^{89}Zr-dSiO$_2$. (e) TEM image of ^{89}Zr-MSN. (f) *In vivo* serial coronal maximum intensity projection PET images of mice at different time points after i.v. injection of ^{89}Zr-MSN. (g) Schematic illustration of ^{89}Zr-MSN. (h) Biodistribution study of ^{89}Zr-MSN on day 21 p.i.

form a small fraction of the total labeled activity (due to much higher internal surface area in each MSN[29]). Since the coordination between silanol groups and ^{89}Zr^{4+} ions is expected to be weaker on the outer surface (due to fewer surrounding silanol groups) than inside the meso-channels, the surface-bound ^{89}Zr^{4+} ions may be rendered more vulnerable to endogenous chelators. Remarkably, the detachment rate of ^{89}Zr from MSN was found to be >20-fold slower than that of ^{89}Zr from dSiO$_2$ (Figure 6b), clearly indicating the vital role of meso-channels in protecting ^{89}Zr from attack by the endogenous chelators. Although ^{89}Zr-labeled MSN using DFO as the chelator has been reported,[21] this is the longest *in vivo* stability study of ^{89}Zr-labeled MSN with such high stability, which could open up a new possibility for studying the long-term fate of MSN-based nanoparticles in live animals.

In addition to the dynamic change of ^{89}Zr uptake in bone, our region of interest (ROI) quantification also provided highly accurate information regarding the accumulation and clearance rate of ^{89}Zr-MSN in mouse liver. Figure 6c shows an increased liver uptake of ^{89}Zr-MSN from 29.7 ± 4.8 %ID/g ($n = 3$) at 0.5 h p.i. to 39.5 ± 4.5 %ID/g on day 7 p.i. For ^{89}Zr-dSiO$_2$, a significant reduction of ^{89}Zr in liver, from 38.1 ± 14.5 to 27.0 ± 0.3 %ID/g due to the lower stability of ^{89}Zr on the surface of dSiO$_2$, was observed over the first 7 days (Table S7). Of note, such dramatic ^{89}Zr uptake change did not correctly reflect the real distribution change of dSiO$_2$ in the liver (*i.e.*, dSiO$_2$ was not cleared from the mouse liver over this time period, but the radio-isotope ^{89}Zr was) and was the main reason for increased ^{89}Zr bone uptake in mice injected with ^{89}Zr-dSiO$_2$, as shown in Figure 5d and 6a (stage 1).

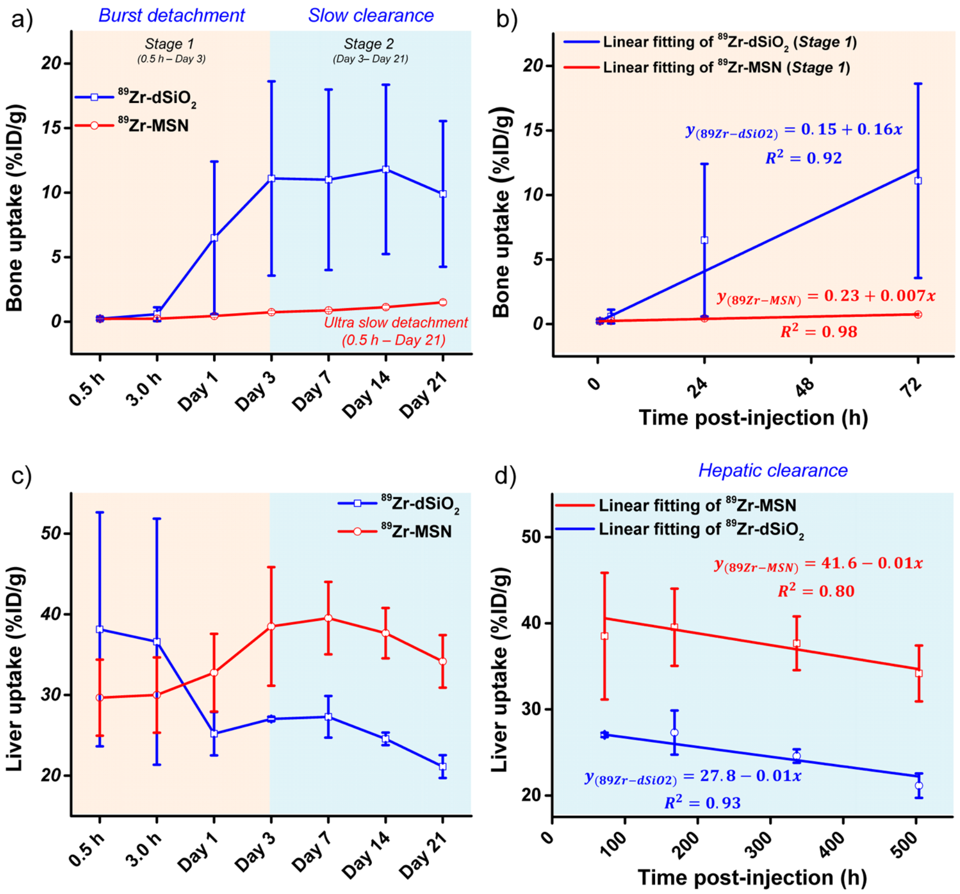

Figure 6. Quantitative region of interest analysis of the dynamic uptake change of ^{89}Zr in bone and liver. Time–activity curves of bone (a) and liver (c) upon i.v. injection of ^{89}Zr-dSiO$_2$ or ^{89}Zr-MSN into BALB/c mice over 21 days. Linear fitting of ^{89}Zr in (b) bone during stage 1 and (d) liver during stage 2.

The hepatic clearance of ^{89}Zr-MSN was also observed with a gradual decrease in liver uptake to 34.2 ± 3.3 %ID/g on day 21 p.i. (Figure 6c and Table S7). Interestingly, we found the same hepatic clearance rate for both ^{89}Zr-dSiO$_2$ and ^{89}Zr-MSN from day 3 to day 21, with their linear fitting slopes both estimated to be −0.01 (Figure 6d). Dominant liver/spleen uptake of ^{89}Zr-MSN and ^{89}Zr-dSiO$_2$ (as expected for i.v. injected nanoparticles) and significantly higher bone uptake of free ^{89}Zr detached from the dSiO$_2$ surface (but not from MSN) were further confirmed in the *ex vivo* biodistribution studies on day 21 p.i. (Figure 5b,h and Table S8).

Renal clearance of porous silicon (130–180 nm in diameter) after degradation *in vivo* has been previously reported.[34] MSN with an average pore size larger than 5 nm has been reported to have a decent (within 3 days) degradation rate *in vitro*.[28] Neither bladder nor kidney uptake of ^{89}Zr-MSN (average pore size: 9–10 nm, Figure 4 and Figure 5f) fragments was observed in this study. Without PEGylation, ^{89}Zr-MSN with a highly negatively charged surface was expected to be accumulated in liver and spleen shortly.

Although bare (unmodified/non-PEGylated) silica nanoparticles were used here in order to better study the chelator-free radio-labeling mechanism and *in vivo* long-term stability, suitable surface functionalization is needed before they can be considered as drug delivery systems. Our pilot studies have successfully demonstrated the *in vivo* tumor active targeting of porous-silica-based nanoparticles (*e.g.*, hollow mesoporous silica nanoparticle or yolk/shell structured nanoparticle), by modifying nanoparticles with polyethylene glycol (PEG) (molecular weight: 5 kDa) and targeting ligands (*e.g.*, TRC105, an anti-CD105 antibody; or YY146, an anti-CD146 antibody) (unpublished data).

We also believe the use of intrinsic deprotonated silanol groups from MSN (or other mesoporous silica-coated nanoparticles) for chelator-free radio-labeling may be applicable to other oxophilic radio-metals, such as titanium-45 (^{45}Ti, $t_{1/2} = 184.8$ m), scandium-44 (^{44}Sc, $t_{1/2} = 3.97$ h), indium-111 (^{111}In, $t_{1/2} = 2.8$ d), yttrium-90 (^{90}Y, $t_{1/2} = 64.0$ h), to name a few. Considering that PEGylated MSN can only circulate in the blood for a couple of hours (depending on the particle size, surface charge, and PEG density, *etc.*), ^{89}Zr with a half-life greater than 3 days might not be the best isotope for short-term PET imaging studies. However, thanks to the general applicability of the as-proposed labeling mechanism, other short-lived oxophilic radio-metals (such as ^{45}Ti and ^{44}Sc) could be used for better matching the biological half-life of PEGylated MSN. Silica-based chelator-free ^{89}Zr labeling can also benefit other applications, such as systematic and long-term *in vivo* biodegradation and biodistribution tracking of MSN (with varied particle and pore sizes), which could provide highly valuable information regarding the *in vivo* fate, potential toxicity, drug delivery, and chemotherapeutic efficacy of MSN in the near future.

CONCLUSIONS

In conclusion, herein we report a chelator-free technique to stably label ^{89}Zr to MSN. Systematic studies demonstrated the vital role of deprotonated silanol groups during the labeling of ^{89}Zr to amorphous porous and nonporous silica nanoparticles. ^{89}Zr labeling yield was concentration- and temperature-dependent, where higher silica concentration and higher incubation temperature gave higher ^{89}Zr labeling yield. *In vitro* DFO challenge and serum stability studies demonstrated the strong binding affinity of ^{89}Zr to both MSN and dSiO$_2$ with nearly negligible ^{89}Zr detachment within 48 h. Remarkably, ^{89}Zr-MSN exhibited high *in vivo* stability with very little bone uptake over 3 weeks. The detachment rate of ^{89}Zr from MSN's meso-channels was further found to be >20-fold slower than that of ^{89}Zr from the dSiO$_2$ surface *in vivo*, highlighting the vital role of meso-channels in stabilizing ^{89}Zr inside MSN.

Considering that silica (or silicon dioxide) is “generally recognized as safe” by the Food and Drug Administration (ID Code: 14808-60-7),[35] which is highly desirable for future clinical translation, and silica coating has been widely used in biomedical applications,[36,37] the as-developed labeling technique might provide a simpler yet more reliable method for theranostic application of future silica-based radio-labeled nanoparticles.

MATERIALS AND METHODS

^{89}Zr Production. ^{89}Zr-oxalate was produced according to our previous procedures by the University of Wisconsin—Madison cyclotron group.[38] Briefly, natural yttrium-89 (^{89}Y) foil (250 μm, 99.9%) was irradiated with a proton beam to create ^{89}Zr *via* the ^{89}Y(p,n)^{89}Zr reaction by using a 16 MeV GE PETtrace cyclotron. After isotope separation and purification, ^{89}Zr-oxalate was obtained, which has a specific activity of >20 GBq/μmol of Zr.

Synthesis of Dense Silica Nanoparticles (dSiO$_2$). Uniform ~90 nm sized dSiO$_2$ was prepared using a modified Stöber method.[39] In a typical synthesis, 35.7 mL of absolute ethanol was mixed with 5 mL of water and 0.8 mL of ammonia and stirred for 5−10 min at room temperature. One milliliter of TEOS was then added, and the mixture was allowed to react at room temperature for 1 h. Afterward, dSiO$_2$ nanoparticles were collected by centrifugation (at 12 500*g* for 10 min), washed with water/ethanol three times, and resuspended in 20 mL of water before use.

Synthesis of Mesoporous Silica Nanoparticles. A previously reported biphase stratification approach with slight modifications was used for the synthesis of MSN with varied pore sizes.[28] In a typical synthesis of ~150 nm sized MSN with 4−5 nm pore size, 24 mL of hexadecyltrimethylammonium chloride (CTAC, 25 wt %) solution and 0.18 g of triethylamine (TEA) were added to 36 mL of water and stirred gently at 60 °C for 3 h in a 100 mL round-bottom flask. Twenty milliliters of (20% v/v) TEOS in cyclohexane was carefully added to the water−CTAC−TEA solution and kept at 60 °C in a water bath for 12 h (stirring rate was set to 125 rpm). Afterward, milky white samples were collected by centrifugation (at 12 500*g* for 10 min), which were subjected to the CTAC removal process by stirring in 1 wt % NaCl/methanol solution three times (24 h/time). Complete removal of CTAC was demonstrated by using Fourier transform infrared spectroscopy.

For the synthesis of MSN with 9−10 nm pore size, the upper organic layer was replaced with 20 mL of (5% v/v) TEOS in cyclohexane. The mixture was reacted at 60 °C in a water bath for 60 h before the CTAC removal process.

Chelator-Free ^{89}Zr Labeling Using dSiO$_2$. For ^{89}Zr labeling, 250 μL of dSiO$_2$ (concentration range: 2 mg/mL to 2×10^{-4} mg/mL) in HEPES buffer (pH 7.5, 0.1 M) was directly mixed with 3 mCi (or 111 MBq) of ^{89}Zr-oxalate at 37 °C (or 75 °C). The final pH value of the mixture was adjusted to 7−8 by using 2 M Na$_2$CO$_3$. ^{89}Zr labeling yield was monitored and quantified at different time points (from 30 min to 2 h) by using thin layer chromatography (TLC). ^{89}Zr-dSiO$_2$ could be easily collected by centrifugation (at 21 000*g* for 10 min).

Chelator-Free ^{89}Zr Labeling Using MSN. For ^{89}Zr labeling, 250 μL of MSN (concentration range: 2 mg/mL to 2×10^{-4} mg/mL) in HEPES buffer (pH 7.5, 0.1 M) was simply mixed with 3 mCi (or 111 MBq) of ^{89}Zr-oxalate at 37 °C (or 75 °C). The final pH value of the mixture was adjusted to 7−8 by using 2 M Na$_2$CO$_3$. ^{89}Zr labeling yield was monitored and quantified at different time points (from 30 min to 2 h) by using radio-TLC. ^{89}Zr-MSN could be easily collected by centrifugation (at 21 000*g* for 10 min).

DFO Challenge Study. To demonstrate the stability of ^{89}Zr in MSN and dSiO$_2$, DFO-Bz-NCS (*p*-isothiocyanatobenzyl desferrioxamine B) with varied concentrations was added into 250 μL of ^{89}Zr-MSN (~200 μCi) or ^{89}Zr-dSiO$_2$ (~200 μCi) HEPES solution (pH 7−8) at 37 °C under constant shaking (550 rpm) for 48 h. The final DFO concentrations were fixed to be 5, 0.5, and 0.05 mM. At each time point, 10 μL of mixture was taken out and resuspended in 200 μL of HEPES. A 100 kDa filter was used to separate potential ^{89}Zr-DFO from ^{89}Zr-labeled nanoparticles. The ^{89}Zr-DFO radio-activity was measured by using a gamma counter (PerkinElmer).

EDTA Challenge Study. To further demonstrate the radiostability of ^{89}Zr in MSN, as-synthesized ^{89}Zr-MSN was soaked in 1 mM EDTA and kept at 37 °C under constant shaking (550 rpm) for 1 week. Both free ^{89}Zr and ^{89}Zr-MSN were monitored and quantified at different time points (from day 1 to day 7) by using radio-TLC. ^{89}Zr-EDTA migrates along the iTLC strip, while ^{89}Zr-MSN remains at the origin.

Loading MSN and ^{89}Zr-MSN with Hydrophilic Anticancer Drugs. Doxorubicin hydrochloride (DOX) was selected as the model drug to test the drug loading capacity of MSN before and after ^{89}Zr labeling. MSN (size: 150 nm; surface area: 581.5 m^2/g; pore volume: 1.31 cm^3/g) with a known mass (0.5 mg) was resuspended in 1 mL (0.5 mg/mL) of DOX-PBS solution (total amount of DOX was 0.5 mg). The mixture was kept under constant shaking for 48 h at room temperature. Afterward, MSN(DOX) was collected by centrifugation (at 21 000*g* for 10 min) and washed with PBS three times. All DOX in the supernatant was carefully collected and quantified based on the DOX (in PBS solution) standard curve. The loading capacity was calculated by the following equation:

$$\text{loading capacity } \% = \text{amount of DOX in MSN/mass of MSN} \times 100$$

To load DOX into ^{89}Zr-MSN, the same amount of MSN (0.5 mg) was first labeled with ^{89}Zr as described previously and then went through the same drug loading process as MSN(DOX). More details about the drug loading can be found in Table S4.

***In Vitro* Serum Stability Study.** To study the *in vitro* serum stability of both ^{89}Zr-dSiO$_2$ and ^{89}Zr-MSN, 50 μL of ^{89}Zr-MSN (or ^{89}Zr-dSiO$_2$) was mixed with 50 μL of 2x whole mouse serum at 37 °C under constant shaking (550 rpm) for 48 h. At each time point, a small fraction of the mixture (15 μL) was collected, resuspended in 100 μL of PBS, and purified by using a 100 kDa filter. The ^{89}Zr activity of the filtrate and that retained in the filter was measured by using a gamma counter.

***In Vivo* PET Imaging of ^{89}Zr-dSiO$_2$ and ^{89}Zr-MSN.** For *in vivo* PET imaging, 150 μL ($\sim$400 μCi or 14.8 MBq) of ^{89}Zr-MSN (or ^{89}Zr-dSiO$_2$) in water was i.v. injected into healthy BALB/c mice ($n = 3$). PET scans at various time points p.i., from 0.5 h to 21 days, were performed by using a microPET/microCT Inveon rodent model scanner (Siemens Medical Solutions USA, Inc.). The images were reconstructed using a maximum a posteriori algorithm, with no scatter correction. ROI analysis of each PET scan was performed using vendor software (Inveon Research Workplace [IRW]) on decay-corrected whole-body images, as we described previously,[40] to calculate the percentage injected dose per gram of tissue (%ID/g) values in mouse liver and bone.

***Ex Vivo* Biodistribution of ^{89}Zr-dSiO$_2$ and ^{89}Zr-MSN.** Biodistribution studies were also carried out to confirm that the quantitative uptake values based on PET imaging truly represented the radio-activity distribution in mice. After the last *in vivo* PET imaging on day 21 p.i., all major organs/tissues were collected and wet-weighed. The radio-activity in the tissue was measured using a gamma counter and presented as %ID/g.

Characterizations. Transmission electron microscopy images were obtained on a FEI T12 microscope operated at an accelerating voltage of 120 kV. Standard TEM samples were prepared by dropping dilute products onto carbon-coated copper grids. Nitrogen adsorption–desorption isotherms were measured at 77 K using a Quantachrome Autosorb-1 system. The samples were pretreated under a vacuum at 393 K for 24 h. Surface areas were determined using the BET method. Pore size distribution data were collected by the Barrett–Joyner–Halenda method of the desorption branch of the isotherm. ζ-Potential analysis was performed on Nano-Zetasizer (Malvern Instruments Ltd.).

Conflict of Interest: The authors declare no competing financial interest.

Supporting Information Available: The Supporting Information is available free of charge on the ACS Publications website at DOI: 10.1021/acsnano.5b00526.

Video S1 (AVI)
Video S2 (AVI)
Temperature- and pH-dependent ^{89}Zr labeling to MSN, maximum intensity projection images of mice injected with free ^{89}Zr-oxalate, labeling yields of ^{89}Zr-MSN and ^{89}Zr-dSiO$_2$, ROI quantification data of ^{89}Zr-dSiO$_2$ and ^{89}Zr-MSN uptake in bone and liver, *ex vivo* biodistribution data of ^{89}Zr-dSiO$_2$ and ^{89}Zr-MSN on Day 21 postinjection, calculation of number of silanol groups per MSN particle (PDF)

Acknowledgment. This work is supported, in part, by the University of Wisconsin—Madison, the National Institutes of Health (NIBIB/NCI 1R01CA169365, P30CA014520, and 5T32GM08349), the National Science Foundation (DGE-1256259), the Department of Defense (W81XWH-11-1-0644), and the American Cancer Society (125246-RSG-13-099-01-CCE).

REFERENCES AND NOTES

1. Hong, H.; Chen, F.; Cai, W. Pharmacokinetic Issues of Imaging with Nanoparticles: Focusing on Carbon Nanotubes and Quantum Dots. *Mol. Imaging Biol.* **2013**, *15*, 507–520.
2. Thakor, A. S.; Gambhir, S. S. Nanooncology: The Future of Cancer Diagnosis and Therapy. *Ca-Cancer J. Clin.* **2013**, *63*, 395–418.
3. Lee, S. B.; Kim, H. L.; Jeong, H. J.; Lim, S. T.; Sohn, M. H.; Kim, D. W. Mesoporous Silica Nanoparticle Pretargeting for PET Imaging Based on a Rapid Bioorthogonal Reaction in a Living Body. *Angew. Chem., Int. Ed.* **2013**, *52*, 10549–10552.
4. Kim, D. W. Bioorthogonal Click Chemistry for Fluorine-18 Labeling Protocols under Physiologically Friendly Reaction Condition. *J. Fluorine Chem.* **2015**, *174*, 142–147.
5. Liu, Z.; Cai, W.; He, L.; Nakayama, N.; Chen, K.; Sun, X.; Chen, X.; Dai, H. *In Vivo* Biodistribution and Highly Efficient Tumour Targeting of Carbon Nanotubes in Mice. *Nat. Nanotechnol.* **2007**, *2*, 47–52.
6. Cai, W.; Chen, K.; Li, Z. B.; Gambhir, S. S.; Chen, X. Dual-Function Probe for PET and Near-Infrared Fluorescence Imaging of Tumor Vasculature. *J. Nucl. Med.* **2007**, *48*, 1862–1870.
7. Yang, X.; Hong, H.; Grailer, J. J.; Rowland, I. J.; Javadi, A.; Hurley, S. A.; Xiao, Y.; Yang, Y.; Zhang, Y.; Nickles, R. J.; et al. cRGD-Functionalized, DOX-Conjugated, and ^{64}Cu-Labeled Superparamagnetic Iron Oxide Nanoparticles for Targeted Anticancer Drug Delivery and PET/MR Imaging. *Biomaterials* **2011**, *32*, 4151–4160.
8. Chen, F.; Hong, H.; Zhang, Y.; Valdovinos, H. F.; Shi, S.; Kwon, G. S.; Theuer, C. P.; Barnhart, T. E.; Cai, W. *In Vivo* Tumor Targeting and Image-Guided Drug Delivery with Antibody-Conjugated, Radiolabeled Mesoporous Silica Nanoparticles. *ACS Nano* **2013**, *7*, 9027–9039.
9. Chen, F.; Ehlerding, E. B.; Cai, W. Theranostic Nanoparticles. *J. Nucl. Med.* **2014**, *55*, 1919–1922.
10. Hong, H.; Zhang, Y.; Sun, J.; Cai, W. Molecular Imaging and Therapy of Cancer with Radiolabeled Nanoparticles. *Nano Today* **2009**, *4*, 399–413.
11. Wang, Y.; Liu, Y.; Luehmann, H.; Xia, X.; Brown, P.; Jarreau, C.; Welch, M.; Xia, Y. Evaluating the Pharmacokinetics and *in Vivo* Cancer Targeting Capability of Au Nanocages by Positron Emission Tomography Imaging. *ACS Nano* **2012**, *6*, 5880–5888.
12. Goel, S.; Chen, F.; Ehlerding, E. B.; Cai, W. Intrinsically Radiolabeled Nanoparticles: An Emerging Paradigm. *Small* **2014**, *10*, 3825–3830.
13. Cheng, L.; Yang, K.; Chen, Q.; Liu, Z. Organic Stealth Nanoparticles for Highly Effective *in Vivo* Near-Infrared Photothermal Therapy of Cancer. *ACS Nano* **2012**, *6*, 5605–5613.
14. Chen, F.; Ellison, P. A.; Lewis, C. M.; Hong, H.; Zhang, Y.; Shi, S.; Hernandez, R.; Meyerand, M. E.; Barnhart, T. E.; Cai, W. Chelator-Free Synthesis of a Dual-Modality PET/MRI Agent. *Angew. Chem., Int. Ed.* **2013**, *52*, 13319–13323.
15. Chakravarty, R.; Valdovinos, H. F.; Chen, F.; Lewis, C. M.; Ellison, P. A.; Luo, H.; Meyerand, M. E.; Nickles, R. J.; Cai, W. Intrinsically Germanium-69-Labeled Iron Oxide Nanoparticles: Synthesis and *in-Vivo* Dual-Modality PET/MR Imaging. *Adv. Mater.* **2014**, *26*, 5119–5123.
16. Zhou, M.; Zhang, R.; Huang, M.; Lu, W.; Song, S.; Melancon, M. P.; Tian, M.; Liang, D.; Li, C. A Chelator-Free Multifunctional [^{64}Cu]CuS Nanoparticle Platform for Simultaneous Micro-PET/CT Imaging and Photothermal Ablation Therapy. *J. Am. Chem. Soc.* **2010**, *132*, 15351–15358.
17. Zhou, J.; Yu, M.; Sun, Y.; Zhang, X.; Zhu, X.; Wu, Z.; Wu, D.; Li, F. Fluorine-18-Labeled Gd^{3+}/Yb^{3+}/Er^{3+} Co-Doped NaYF$_4$ Nanophosphors for Multimodality PET/MR/UCL Imaging. *Biomaterials* **2011**, *32*, 1148–1156.
18. Jauregui-Osoro, M.; Williamson, P. A.; Glaria, A.; Sunassee, K.; Charoenphun, P.; Green, M. A.; Mullen, G. E.; Blower, P. J. Biocompatible Inorganic Nanoparticles for [^{18}F]-Fluoride Binding with Applications in PET Imaging. *Dalton Trans.* **2011**, *40*, 6226–6237.
19. Zhang, Y.; Hong, H.; Cai, W. PET Tracers Based on Zirconium-89. *Curr. Radiopharm.* **2011**, *4*, 131–139.
20. Manchun, S.; Dass, C. R.; Sriamornsak, P. Targeted Therapy for Cancer Using pH-Responsive Nanocarrier Systems. *Life Sci.* **2012**, *90*, 381–387.
21. Miller, L.; Winter, G.; Baur, B.; Witulla, B.; Solbach, C.; Reske, S.; Linden, M. Synthesis, Characterization, and Biodistribution of Multiple ^{89}Zr-Labeled Pore-Expanded Mesoporous Silica Nanoparticles for Pet. *Nanoscale* **2014**, *6*, 4928–4935.
22. Chang, A. J.; Desilva, R.; Jain, S.; Lears, K.; Rogers, B.; Lapi, S. ^{89}Zr-Radiolabeled Trastuzumab Imaging in Orthotopic and Metastatic Breast Tumors. *Pharmaceuticals* **2012**, *5*, 79–93.
23. Aerts, H. J.; Dubois, L.; Perk, L.; Vermaelen, P.; van Dongen, G. A.; Wouters, B. G.; Lambin, P. Disparity between *in Vivo* EGFR Expression and ^{89}Zr-Labeled Cetuximab Uptake Assessed with PET. *J. Nucl. Med.* **2009**, *50*, 123–131.

24. Tinianow, J. N.; Gill, H. S.; Ogasawara, A.; Flores, J. E.; Vanderbilt, A. N.; Luis, E.; Vandlen, R.; Darwish, M.; Junutula, J. R.; Williams, S. P.; et al. Site-Specifically ^{89}Zr-Labeled Monoclonal Antibodies for Immunopet. *Nucl. Med. Biol.* **2010**, *37*, 289–297.
25. Holland, J. P.; Divilov, V.; Bander, N. H.; Smith-Jones, P. M.; Larson, S. M.; Lewis, J. S. ^{89}Zr-DFO-J591 for Immunopet of Prostate-Specific Membrane Antigen Expression *in Vivo*. *J. Nucl. Med.* **2010**, *51*, 1293–1300.
26. Chen, Y.; Chen, H.; Shi, J. *In Vivo* Bio-Safety Evaluations and Diagnostic/Therapeutic Applications of Chemically Designed Mesoporous Silica Nanoparticles. *Adv. Mater.* **2013**, *25*, 3144–3176.
27. Zhuravlev, L. T. The Surface Chemistry of Amorphous Silica. Zhuravlev Model. *Colloids Surf., A* **2000**, *173*, 1–38.
28. Shen, D.; Yang, J.; Li, X.; Zhou, L.; Zhang, R.; Li, W.; Chen, L.; Wang, R.; Zhang, F.; Zhao, D. Biphase Stratification Approach to Three-Dimensional Dendritic Biodegradable Mesoporous Silica Nanospheres. *Nano Lett.* **2014**, *14*, 923–932.
29. Slowing, I. I.; Wu, C. W.; Vivero-Escoto, J. L.; Lin, V. S. Mesoporous Silica Nanoparticles for Reducing Hemolytic Activity Towards Mammalian Red Blood Cells. *Small* **2009**, *5*, 57–62.
30. Lin, Y. S.; Haynes, C. L. Impacts of Mesoporous Silica Nanoparticle Size, Pore Ordering, and Pore Integrity on Hemolytic Activity. *J. Am. Chem. Soc.* **2010**, *132*, 4834–4842.
31. Boros, E.; Bowen, A. M.; Josephson, L.; Vasdev, N.; Holland, J. P. Chelate-Free Metal Ion Binding and Heat-Induced Radiolabeling of Iron Oxide Nanoparticles. *Chem. Sci.* **2015**, *6*, 225–236.
32. Meijs, W. E.; Haisma, H. J.; Klok, R. P.; van Gog, F. B.; Kievit, E.; Pinedo, H. M.; Herscheid, J. D. Zirconium-Labeled Monoclonal Antibodies and Their Distribution in Tumor-Bearing Nude Mice. *J. Nucl. Med.* **1997**, *38*, 112–118.
33. Abou, D. S.; Ku, T.; Smith-Jones, P. M. *In Vivo* Biodistribution and Accumulation of ^{89}Zr in Mice. *Nucl. Med. Biol.* **2011**, *38*, 675–681.
34. Park, J. H.; Gu, L.; von Maltzahn, G.; Ruoslahti, E.; Bhatia, S. N.; Sailor, M. J. Biodegradable Luminescent Porous Silicon Nanoparticles for *in Vivo* Applications. *Nat. Mater.* **2009**, *8*, 331–336.
35. http://www.fda.gov/Food/IngredientsPackagingLabeling/GRAS/ (accessed July 22, 2015).
36. Wang, K.; He, X.; Yang, X.; Shi, H. Functionalized Silica Nanoparticles: A Platform for Fluorescence Imaging at the Cell and Small Animal Levels. *Acc. Chem. Res.* **2013**, *46*, 1367–1376.
37. Tallury, P.; Payton, K.; Santra, S. Silica-Based Multimodal/Multifunctional Nanoparticles for Bioimaging and Biosensing Applications. *Nanomedicine (London, U. K.)* **2008**, *3*, 579–592.
38. Zhang, Y.; Hong, H.; Severin, G. W.; Engle, J. W.; Yang, Y.; Goel, S.; Nathanson, A. J.; Liu, G.; Nickles, R. J.; Leigh, B. R.; et al. Immunopet and Near-Infrared Fluorescence Imaging of CD105 Expression Using a Monoclonal Antibody Dual-Labeled with ^{89}Zr and IRdye 800CW. *Am. J. Transl. Res.* **2012**, *4*, 333–346.
39. Chen, Y.; Chen, H.; Guo, L.; He, Q.; Chen, F.; Zhou, J.; Feng, J.; Shi, J. Hollow/Rattle-Type Mesoporous Nanostructures by a Structural Difference-Based Selective Etching Strategy. *ACS Nano* **2010**, *4*, 529–539.
40. Hong, H.; Yang, Y.; Zhang, Y.; Engle, J. W.; Barnhart, T. E.; Nickles, R. J.; Leigh, B. R.; Cai, W. Positron Emission Tomography Imaging of CD105 Expression During Tumor Angiogenesis. *Eur. J. Nucl. Med. Mol. Imaging* **2011**, *38*, 1335–1343.